

## Controlling Feynman diagrammatic expansions: Physical nature of the pseudogap in the two-dimensional Hubbard model

Wei Wu,<sup>1,2</sup> Michel Ferrero,<sup>1,2</sup> Antoine Georges,<sup>2,1,3</sup> and Evgeny Kozik<sup>4</sup>

<sup>1</sup>*Centre de Physique Théorique, École Polytechnique, CNRS, Université Paris-Saclay, 91128 Palaiseau, France*

<sup>2</sup>*Collège de France, 11 place Marcelin Berthelot, 75005 Paris, France*

<sup>3</sup>*DQMP, Université de Genève, 24 quai Ernest Ansermet, CH-1211 Genève, Switzerland*

<sup>4</sup>*Physics Department, King's College London, Strand, London WC2R 2LS, United Kingdom*

(Received 24 August 2016; published 6 July 2017)

We introduce a method for summing Feynman's perturbation series based on diagrammatic Monte Carlo that significantly improves its convergence properties. This allows us to investigate in a controllable manner the pseudogap regime of the Hubbard model and to study the nodal/antinodal dichotomy at low doping and intermediate coupling. Marked differences from the weak-coupling scenario are manifest, such as a higher degree of incoherence at the antinodes than at the “hot spots”. Our results show that the pseudogap and reduction of quasiparticle coherence at the antinode is due to antiferromagnetic spin correlations centered around the commensurate  $(\pi, \pi)$  wave vector. In contrast, the dominant source of scattering at the node is associated with incommensurate momentum transfer. Umklapp scattering is found to play a key role in the nodal/antinodal dichotomy.

DOI: [10.1103/PhysRevB.96.041105](https://doi.org/10.1103/PhysRevB.96.041105)

### I. INTRODUCTION

Strongly correlated many-electron systems are a major theoretical challenge. Numerical approaches face difficulties brought by the exponentially large Hilbert space or the fermionic sign problem. Among the many questions still open, an outstanding one is the nature of the low doping and intermediate- to strong-coupling regime of the prototypical two-dimensional Hubbard model. Unbiased methods are needed to establish whether key aspects of cuprate phenomenology, such as the opening of a pseudogap and the associated nodal/antinodal (N/AN) dichotomy [1,2], are intrinsic features of the model, and to settle the much debated physical origin of these phenomena. Recently, cluster-dynamical mean-field theory (DMFT) approaches have allowed significant progress on these issues [3–6]. However, cluster methods lack fine momentum resolution [7], which is crucial in view of the strong momentum dependence along the Fermi surface, and in establishing which fluctuations are responsible for the physics [8], e.g., distinguishing commensurate and incommensurate fluctuations.

A promising alternative method is the diagrammatic Monte Carlo (DiagMC) technique [9–11], based on the stochastic summation of Feynman diagrammatic series directly in the thermodynamic limit, which in principle enables controlled solutions with arbitrary momentum resolution. However, for lattice systems, fundamental problems with series convergence have so far limited its scope of application to modest couplings, relatively high temperature, and/or low density. In particular, the skeleton series built on the full (interacting) Green's function  $G$  can converge to a wrong answer [12], whereas the bare series built on the noninteracting Green's function  $G_0$  does not exhibit misleading convergence but typically diverges in the strongly correlated regime.

In this Rapid Communication, we introduce an approach that considerably enlarges the applicability range of DiagMC. It is based on a parametric modification of the bare diagrammatic series that improves its convergence properties. This

technique allows us to address the pseudogap regime of the two-dimensional (2D) Hubbard model at small doping and intermediate coupling. The high momentum resolution and direct access to scattering processes in DiagMC allow us to identify the physical origins of the pseudogap and N/AN dichotomy, which are shown to result from antiferromagnetic spin correlations. At the node, the transfer momentum  $\mathbf{q}$  of relevant modes is found to be incommensurate, connecting Fermi surface points. In contrast, at the antinode, scattering with commensurate momentum exchange  $\mathbf{q} = (\pi, \pi)$  dominates. We find that quasiparticles are more incoherent at the antinode than at the “hot spots” (where the Fermi surface intersects the antiferromagnetic zone boundary), thus establishing the strong-coupling nature of the regime investigated. We show that the umklapp scattering enhanced at large perturbation orders plays a key role in this suppression of coherence.

### II. THE METHOD: ACTION OPTIMIZATION AND RECURSIVE EVALUATION OF DIAGRAMS

We study the Hubbard model on an (infinite) square lattice,

$$\mathcal{H} = - \sum_{ij\sigma} t_{ij} c_{i\sigma}^\dagger c_{j\sigma} + U \sum_i n_{i\uparrow} n_{i\downarrow}, \quad (1)$$

with hopping amplitudes  $t$  and  $t'$  between nearest-neighbor and next-nearest-neighbor sites, respectively, and use  $t = 1$  as our energy unit. In essence, DiagMC is an efficient way of computing the coefficients  $a_l$  of a perturbative series for the self-energy as a function of the Matsubara frequency  $\omega_n$  and momentum  $\mathbf{k}$ ,

$$\Sigma(i\omega_n, \mathbf{k}) = \lim_{L \rightarrow \infty} \sum_{l=1}^L a_l(i\omega_n, \mathbf{k}) U^l, \quad (2)$$

where  $a_l$  is a sum of all one-particle irreducible (1PI) Feynman diagrams with  $l$  interaction vertices connected by noninteracting Green's functions  $G_0(i\omega_n, \mathbf{k}) = [i\omega_n - \epsilon_{\mathbf{k}} + \mu]^{-1}$  [13]. The success of this approach fundamentally relies on

the convergence properties of the series (2). Because  $a_l$  are stochastically computed in DiagMC as the sums of the factorial (in  $l$ ) number of sign-alternating contributions, in practice one can only reach  $L = 6-7$  with reasonable statistical error bars due to the fermionic sign problem. Thus, a controlled answer is only warranted as long as the series (2) can be reliably extrapolated to  $L \rightarrow \infty$  given an essentially limited number of computed expansion orders. This extrapolation becomes increasingly difficult at low  $T$  and large  $U$ .

In order to establish control over the convergence properties of the series, we introduce a modified action  $S_\xi$  given by

$$S_\xi = - \sum_{\omega_n, \mathbf{k}, \sigma} c_{\omega_n, \mathbf{k}, \sigma}^\dagger \tilde{G}_0(i\omega_n, \mathbf{k})^{-1} c_{\omega_n, \mathbf{k}, \sigma} - \xi \sum_{\omega_n, \mathbf{k}, \sigma} \alpha_{\mathbf{k}}(i\omega_n) c_{\omega_n, \mathbf{k}, \sigma}^\dagger c_{\omega_n, \mathbf{k}, \sigma} + \xi U \int_0^\beta n_{\tau \uparrow} n_{\tau \downarrow} d\tau, \quad (3)$$

where  $\tilde{G}_0(i\omega_n, \mathbf{k})^{-1} = i\omega_n + \mu - \epsilon_{\mathbf{k}} - \alpha_{\mathbf{k}}(i\omega_n) = G_0(i\omega_n, \mathbf{k})^{-1} - \alpha_{\mathbf{k}}(i\omega_n)$  and  $\alpha_{\mathbf{k}}(i\omega_n)$  is an arbitrary auxiliary field. When  $\xi = 1$ , we recover the original action for the Hamiltonian (1). The freedom in choosing the noninteracting propagator  $\tilde{G}_0(i\omega_n, \mathbf{k})$  has been employed by several authors in the contexts of many-body perturbation theory (see, e.g., Refs. [14–19]). Expanding in powers of  $\xi$  and applying Wick's theorem generates a new diagrammatic representation of  $\Sigma$ ,

$$\Sigma(i\omega_n, \mathbf{k}) = \lim_{M \rightarrow \infty} \sum_{m=1}^M \tilde{a}_m(i\omega_n, \mathbf{k}) \xi^m. \quad (4)$$

Here, the coefficient  $\tilde{a}_m$  is a sum of all the diagrams for  $a_l$  with  $l$  running from 1 to  $m$ , and for each diagram of order  $l$ , an additional sum over all possible ways of inserting  $m - l$  instances of  $\alpha_{\mathbf{k}}(i\omega_n)$  in the fermionic lines is performed according to the standard diagrammatic rules of expanding with respect to an external field [13]. Note that here the bare propagators  $G_0(i\omega_n, \mathbf{k})$  are now replaced with  $\tilde{G}_0(i\omega_n, \mathbf{k})$ . The freedom in choosing  $\alpha_{\mathbf{k}}(i\omega_n)$  can be now used to control the convergence properties of the modified series (4) at  $\xi = 1$ , as recently done in a real-time algorithm [18].

This freedom comes at the expense of extending the diagrammatic space, which considerably worsens the sign problem. To make practical calculations feasible we introduce a recursive protocol for summing all the diagrams for  $\tilde{a}_m$ , which makes use of the already computed  $\tilde{a}_n$ ,  $n < m$ . The idea is that a high-order diagram may contain (between propagator lines) self-energy insertions of lower orders; all possible insertions of the total order  $p$  can be implicitly summed and integrated over the internal momentum/frequency variables by including the results for  $\tilde{a}_n$ ,  $n \leq p$ , in the propagator lines,

$$G^{(p)} = \sum_{n=0}^p G^{(n)} \tilde{a}_{p-n} \xi^{p-n} \tilde{G}_0, \quad p > 0, \quad G^{(0)} \equiv \tilde{G}_0, \quad (5)$$

so that  $G^{(p)} \propto \xi^p$ . Then,  $\tilde{a}_m$  can be obtained by DiagMC sampling of only 1PI skeleton diagrams of order  $l = \{1, \dots, m\}$ , where in each diagram some bare propagators  $\tilde{G}_0$  are randomly replaced by dressed propagators  $G^{(p)}$  so that  $\sum_i p_i = m - l$ . This recursive approach substantially improves the efficiency

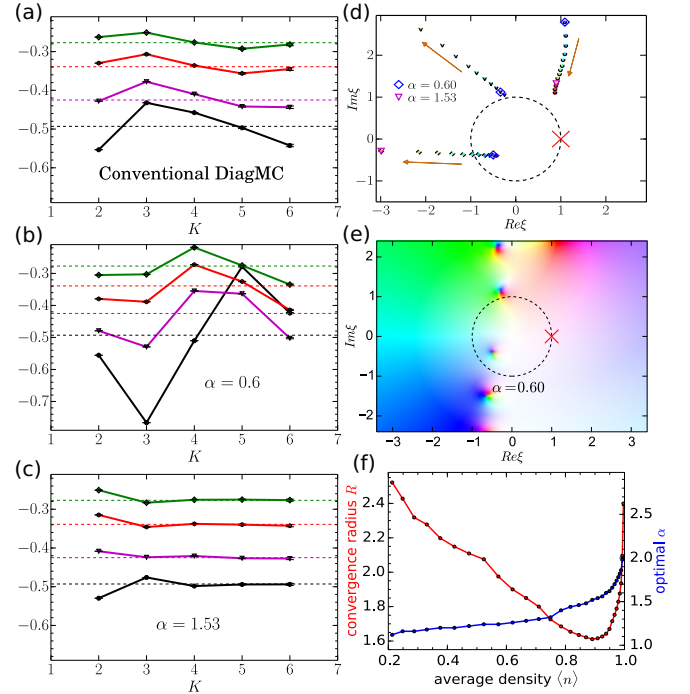


FIG. 1. Left column: Imaginary part of the Hubbard model self-energy at the first four Matsubara frequencies obtained as a sum of the first  $K$  perturbation orders. The parameters are  $U = 4.0$ ,  $t' = -0.3$ ,  $\mu = 0$ ,  $n \sim 0.725$ ,  $T = 0.5$ . The dashed lines are a benchmark from determinantal QMC simulations on a  $16 \times 16$  lattice (the discrete time interval is  $\Delta\tau = 0.0375$ , where the Trotter error is negligible). (a) Standard series with Hartree diagrams included in bare Green's function. (b)  $\alpha$ -shifted case with  $\alpha = 0.6$ . (c) The optimal case  $\alpha = 1.53$ . Right column: Results for the atomic limit  $t = 0$ ,  $U = 4$ ,  $T = 0.5$ ,  $\mu = 0.138$ ,  $n \sim 0.725$ . (e) Modulus/phase (displayed as saturation/hue) map of the self-energy in the complex  $\xi$  plane for  $\alpha = 0.6$ . The physical solution is at the cross  $\xi = 1$  on the unit circle. (d) The arrows and dots show trajectories of three poles as  $\alpha$  is changed from 0.5 to 1.8. (f) Optimal  $\alpha$  and corresponding maximal convergence radius as a function of the density ( $n$ ) in the Hubbard atom.

of DiagMC by effectively reducing the configuration space and can be generalized to other channels, e.g., by introducing dressed interaction lines  $W^{(p)}$ , dressed two-particle irreducible vertices  $\Gamma^{(p)}$ , etc.

### III. ILLUSTRATIVE RESULT AT HIGH $T/t$

We first investigate the simplest case of a constant field  $\alpha_{\mathbf{k}}(i\omega_n) \equiv \alpha$ . In Fig. 1, we illustrate its effect on the Hubbard model at  $U = 4$  and  $T = 0.5$ , using a determinantal quantum Monte Carlo (QMC) simulation on a  $16 \times 16$  lattice as a benchmark [20]. In the first row of Fig. 1, we compare the value of  $\Sigma(\mathbf{k}, i\omega_n)$  at the first few Matsubara frequencies and  $\mathbf{k} = (\pi/4, \pi)$  summed up to order  $K$ , i.e.,  $\Sigma(\mathbf{k}, i\omega_n) = \sum_{m=1}^K \tilde{a}_m(\mathbf{k}, n) \xi^m$ . Figure 1(a) shows the behavior of the standard series (2) (with the Hartree diagrams included in the Green's function following Refs. [10,11]), Figures 1(b) and 1(c) show the behavior for two different choices of  $\alpha$ . Clearly, the standard series and the one for an arbitrarily selected

$\alpha = 0.6$  fail to converge within accessible orders. However, a clever choice of  $\alpha = 1.53$  yields a great improvement of convergence. The exact result is recovered already at order 4 and the extrapolation of the series to infinite order is straightforward.

#### IV. RATIONALE: POLE MOVING

In order to get insight into the improvement brought by the introduction of a modified action, we study in detail the limiting case  $t = 0$ , the Hubbard atom, which can be solved exactly. In particular, we show how tuning  $\alpha$  allows to control the convergence radius of the series (4). The self-energy for the action  $S_\xi$  and  $t = 0$  is given by

$$\Sigma(i\omega_n) = \frac{n\xi U}{2} + \frac{1}{4} \frac{n(2-n)\xi^2 U^2}{i\omega_n + \tilde{\mu} - (2-n)\xi U/2}, \quad (6)$$

$$\tilde{\mu} = \xi\alpha - \alpha + \mu, \quad (7)$$

where  $n = [e^{\beta\tilde{\mu}} + e^{2\beta\tilde{\mu} - \beta\xi U}] / [1 + 2e^{\beta\tilde{\mu}} + e^{2\beta\tilde{\mu} - \beta\xi U}]$  is the density. The analytical structure of  $\Sigma(i\omega_0)$  in the complex- $\xi$  plane is shown in Figs. 1(d) and 1(e). The convergence radius  $R$  of the series expansion in  $\xi$  is given by the distance from the origin to the closest pole in the complex- $\xi$  plane, which strongly depends on the value of  $\alpha$ . For  $\alpha = 0.6$  a pole is closer to the origin than the evaluation point  $\xi = 1$  and the series diverges, whereas for  $\alpha = 1.53$  the poles are further away and the series is convergent at  $\xi = 1$ . When  $\alpha$  is further increased, new poles get closer to the origin and there is therefore an optimal value for  $\alpha$  for which the radius of convergence is maximal. A systematic study for the full Hubbard model at  $T = 0.5$  suggests an optimal value of  $\alpha \simeq 1.53$ , close to this atomic estimate  $\alpha \sim 1.3$ , as expected from a similar analytic structure of  $\Sigma$  at this high temperature. Thus the Hubbard atom can provide a reasonable guide for finding the optimal  $\alpha$ . Finally, we find the largest convergence radius and the corresponding optimal  $\alpha$  for different densities of the Hubbard atom, as displayed in Fig. 1(d). We see that  $R$  is infinite at half filling and becomes finite ( $R \lesssim 2.5$ ) as soon as a doping is introduced. For  $U = 4$ , the convergence radius is always large enough for the series to converge. It has a minimum  $R \simeq 1.6 > 1$  around 10% hole (or electron) doping.

#### V. REACHING THE PSEUDOGAP SCALE

We now show that this improved scheme allows one to reach the pseudogap region [21–24]. We consider the Hubbard model on an infinite square lattice at 4% hole doping and  $U = 5.6$ ,  $t' = -0.3$  [25]. We could achieve convergence down to  $T = 0.2$ , where we compute the self-energy up to seventh order with an optimized  $\alpha = 2.2$ . The average sign at order 7 is about  $10^{-4}$ , which precludes access to higher orders. In Fig. 2, we display the imaginary part of the self-energy  $\text{Im} \Sigma(\mathbf{k}, i\omega_n)$  taken at three different momenta  $\mathbf{k}$  on the Fermi surface (FS). We see that the self-energy behaves differently at the nodal point  $\mathbf{k}_N = (1.47, 1.47)$  (intersection of the FS with the zone diagonal) in comparison to the antinode  $\mathbf{k}_{AN} = (3.04, 0.49)$  (where the FS hits the upper zone boundary). The imaginary part of the AN self-energy extrapolates to a larger negative value at low frequency, indicating the strongest correlation

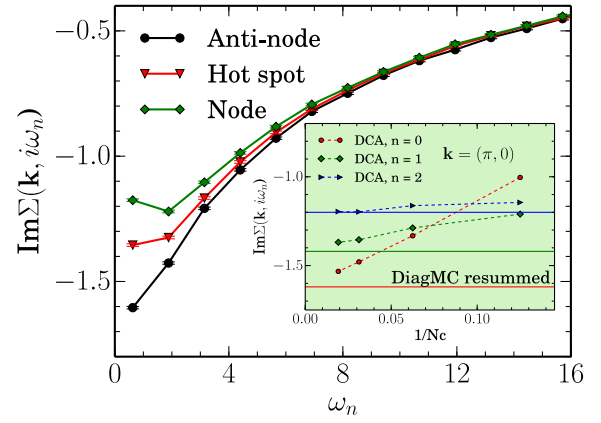


FIG. 2. Imaginary part of the self-energy at the node, hot spot, and antinode at  $U = 5.6$ ,  $t' = -0.3$ ,  $n = 0.96$ ,  $T = 0.2$ . Inset: DCA results with cluster size  $N_c = 8, 16, 32, 52$  extrapolate to the DiagMC-summed result (plain horizontal lines) at different frequencies.

effects at the AN. Hence, a clear N/AN differentiation is already apparent at  $T = 0.2$ , consistently with previous calculations [21,26]. The inset of Fig. 2 also demonstrates that our results at the AN are in excellent agreement with large scale dynamical cluster approximation (DCA) [4] ones (after extrapolating the latter as a function of cluster size). Finally, we note (Fig. 2) that the self-energy is larger at the AN than at the “hot spot”  $\mathbf{k}_{HS} = (2.26, 0.88)$  (intersection of the FS with the antiferromagnetic zone boundary), indicating that we have reached a regime in which the weak-coupling spin-fluctuation picture does not apply. Being able to resolve the difference of behavior at the HS and AN is a clear advantage of the current approach as compared to cluster methods.

#### VI. PHYSICAL ORIGIN OF THE NODAL/ANTINODAL DICHOTOMY: ANTIFERROMAGNETIC SPIN CORRELATIONS

A decisive asset of DiagMC is that it provides direct information about the mechanisms behind the pseudogap and N/AN differentiation. We demonstrate that umklapp processes are essential to the destruction of the AN quasiparticles. To this aim, we decompose the self-energy as shown in Fig. 3(b) and monitor the momentum entering the two-particle scattering amplitude  $F_{\uparrow\downarrow}$  during the DiagMC evaluation. By forcing the sum of incoming and outgoing momenta of  $F_{\uparrow\downarrow}$  to differ by a nonzero or zero reciprocal lattice vector  $G$ , we allow or forbid umklapp scattering at will. The results are given in Fig. 3: When umklapp processes are forbidden, both the imaginary part of N and AN Green’s functions become significantly larger, indicating that umklapp processes are relevant to suppress spectral weight in the full solution. More importantly, without umklapp processes, AN Green’s function turns out to be more coherent than the N one, while the opposite is true when umklapp processes are allowed. They are therefore a key ingredient in the suppression of spectral weight at the AN, and their importance is actually found to grow as the perturbation order increases (not shown).

To analyze further the N/AN dichotomy, we employ the Dyson-Schwinger equation representing the self-energy at a

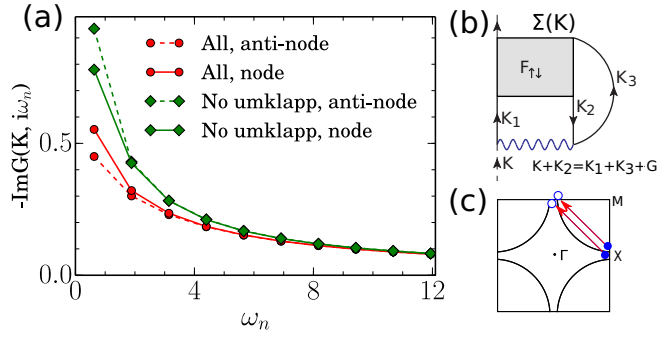


FIG. 3. (a) Imaginary part of the Green's functions at node and antinode as a function of frequency, in cases with and without umklapp processes. (b) Decomposition of the self-energy using the Dyson-Schwinger equation of motion [cf. Eq. 8]. (c) Illustration of a typical weak-coupling umklapp process with  $G = (2\pi, 2\pi)$ .

given momentum  $\mathbf{k}$  as [Fig. 3(b)]

$$\Sigma(\mathbf{k}) = \frac{Un}{2} - \sum_{\mathbf{k}', \mathbf{q}} F_{\uparrow\downarrow}(\mathbf{k}, \mathbf{k}', \mathbf{q}) g(\mathbf{k}) g(\mathbf{k}' + \mathbf{q}) g(\mathbf{k} + \mathbf{q}), \quad (8)$$

or  $\Sigma(\mathbf{k}) = \frac{Un}{2} - \sum_{\mathbf{q}} [\Sigma_X^{\mathbf{q}}(\mathbf{k})]$ , and study the contributions from different collective modes with the transfer momentum  $\mathbf{q}$ , where  $X$  stands for spin (sp), charge (ch), or particle-particle (pp) representations,

$$\begin{aligned} \Sigma_{\text{sp}}^{\mathbf{q}}(\mathbf{k}) &= \sum_{\mathbf{k}'} -F_{\uparrow\downarrow}(\mathbf{k}, \mathbf{k} + \mathbf{q}, \mathbf{k}' - \mathbf{k}) g(\mathbf{k}') g(\mathbf{k}' + \mathbf{q}) g(\mathbf{k} + \mathbf{q}), \\ \Sigma_{\text{ch}}^{\mathbf{q}}(\mathbf{k}) &= \sum_{\mathbf{k}'} [F_{\uparrow\downarrow}(\mathbf{k}, \mathbf{k} + \mathbf{q}, \mathbf{k}' - \mathbf{k}) \\ &\quad - 2 \times F_{\uparrow\downarrow}(\mathbf{k}, \mathbf{k}', \mathbf{q})] g(\mathbf{k}') g(\mathbf{k}' + \mathbf{q}) g(\mathbf{k} + \mathbf{q}), \\ \Sigma_{\text{pp}}^{\mathbf{q}}(\mathbf{k}) &= \sum_{\mathbf{k}'} -F_{\uparrow\downarrow}(\mathbf{k}, \mathbf{k}', \mathbf{q} - \mathbf{k} - \mathbf{k}') g(\mathbf{k}') g(\mathbf{q} - \mathbf{k}') g(\mathbf{q} - \mathbf{k}). \end{aligned} \quad (9)$$

The above equations are obtained by expressing  $F_{\text{sp/ch/pp}}$  in terms of  $F_{\uparrow\downarrow}$  (see Ref. [8]). The resulting low-energy intensity maps of  $\Sigma_X^{\mathbf{q}}(\mathbf{k})$  (obtained at order 7) for all three representations at the N and at the AN are displayed in Fig. 4. The first compelling result is that the charge and the particle-particle representations are essentially featureless for both the N and AN self-energies. The only visible patterns stem from FS to FS transfer momenta, as shown by the light circles. In contrast, the spin channel exhibits dominant modes responsible for the largest contribution to the imaginary part of the self-energy at low energies. Interestingly, the most significant transfer momenta are all close to  $(\pi, \pi)$  and we conclude that antiferromagnetic spin correlations are the leading scattering mechanism in the pseudogap region of the phase diagram, in agreement with recent experimental findings [2,27]. The fine momentum resolution of DiagMC allows us to examine the difference between the N and AN self-energy in further detail. We see that, at the N,

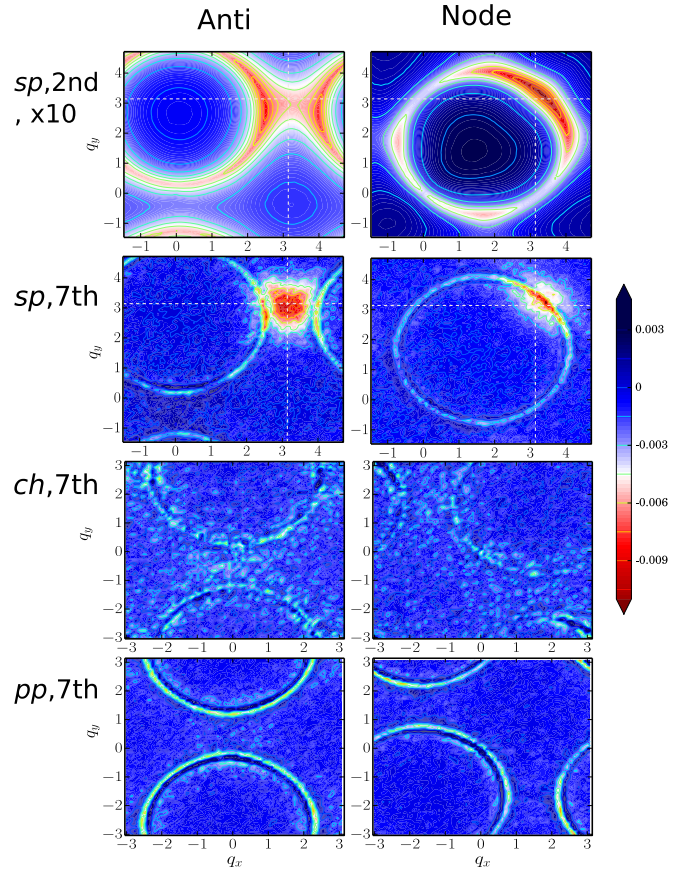


FIG. 4. Maps of the transfer momentum  $\mathbf{q}$  contributions to  $\text{Im} \Sigma(\mathbf{k}, i\omega_0) + \text{Im} \Sigma(\mathbf{k}, i\omega_1)$  in the spin (sp), charge (ch), and particle-particle (pp) channels, both at the antinode,  $\mathbf{k} = (3.04, 0.49)$  (left column), and node,  $\mathbf{k} = (1.47, 1.47)$  (right column). The two panels on the top are results at perturbation order 2 while the rest are obtained up to order 7.

the transfer momenta are close, but not exactly at  $(\pi, \pi)$ . They are concentrated around the Fermi surface and are not exactly commensurate. On the contrary, at the AN the transfer momenta are centered around  $(\pi, \pi)$  and the corresponding amplitude is larger. The existence of a saddle point in the band dispersion (van Hove singularity) close to the AN may be at the origin of this difference, the flatter dispersion allowing one to compensate for the energetic cost of commensurate  $(\pi, \pi)$  spin scattering. The relevance of the saddle point has been discussed in Refs. [28–30] within weak-coupling approaches. Importantly, we note (Fig. 4) that FS scattering involving an incommensurate transfer momentum controls the nodal self-energy at both low and high perturbation orders. In contrast,  $(\pi, \pi)$  scattering emerges at high perturbation orders at the AN. Hence, the scattering mechanism remains of the weak-coupling type at the N, while the pseudogap opening at the AN is a strong-coupling phenomenon for the value of  $U/t$  studied here. From similar calculations for  $4 \leq U/t \leq 6$  and different Fermi surface topologies we observe that the qualitative picture described above is realized as soon as a clear nodal/antinode differentiation sets in. For the value of  $U/t < 4$ , both the scattering at the N and at the AN are

incommensurate and similar to what would be obtained in weak-coupling approaches.

## VII. CONCLUSIONS AND PERSPECTIVES

In this Rapid Communication, we have introduced an improved DiagMC method relying on an optimized parametric modification of the Hubbard model action. This allows us to access in a controlled way and with high momentum resolution parameter regimes that were previously unreachable, such as the onset of the pseudogap and nodal/antinodal differentiation. We show that these effects are due to antiferromagnetic correlations and that marked differences with weak-coupling spin-fluctuation theories appear in the regime of coupling in-

vestigated here. The challenge ahead is to improve the current method in order to reach significantly lower temperatures.

## ACKNOWLEDGMENTS

We would like to thank P. J. Hirschfeld, A. J. Millis, O. Parcollet, N. Prokof'ev, B. Svistunov, N.-H. Tong, and A.-M. S. Tremblay for useful discussions. This work has been supported by the Simons Foundation within the Many Electron Collaboration framework. We also acknowledge support of the European Research Council (Grant No. ERC-319286 QMAC) and of the Swiss National Supercomputing Center (CSCS) under Project No. s575. Some of the calculations were performed with the TRIQS [31] toolbox.

- 
- [1] T. Timusk and B. Statt, *Rep. Prog. Phys.* **62**, 61 (1999).
- [2] S. Badoux, W. Tabis, F. Laliberté, G. Grissonnanche, B. Vignolle, D. Vignolles, J. Béard, D. Bonn, W. Hardy, R. Liang, N. Doiron-Leyraud, L. Taillefer, and C. Proust, *Nature (London)* **531**, 210 (2016).
- [3] A. Georges, G. Kotliar, W. Krauth, and M. J. Rozenberg, *Rev. Mod. Phys.* **68**, 13 (1996).
- [4] T. Maier, M. Jarrell, T. Pruschke, and M. H. Hettler, *Rev. Mod. Phys.* **77**, 1027 (2005).
- [5] D. Sénéchal and A.-M. S. Tremblay, *Phys. Rev. Lett.* **92**, 126401 (2004).
- [6] J. P. F. LeBlanc, A. E. Antipov, F. Becca, I. W. Bulik, G. K.-L. Chan, C.-M. Chung, Y. Deng, M. Ferrero, T. M. Henderson, C. A. Jiménez-Hoyos, E. Kozik, X.-W. Liu, A. J. Millis, N. V. Prokof'ev, M. Qin, G. E. Scuseria, H. Shi, B. V. Svistunov, L. F. Tocchio, I. S. Tupitsyn, S. R. White, S. Zhang, B.-X. Zheng, Z. Zhu, and E. Gull (Simons Collaboration on the Many-Electron Problem), *Phys. Rev. X* **5**, 041041 (2015).
- [7] E. Gull, M. Ferrero, O. Parcollet, A. Georges, and A. J. Millis, *Phys. Rev. B* **82**, 155101 (2010).
- [8] O. Gunnarsson, T. Schäfer, J. P. F. LeBlanc, E. Gull, J. Merino, G. Sangiovanni, G. Rohringer, and A. Toschi, *Phys. Rev. Lett.* **114**, 236402 (2015).
- [9] N. V. Prokof'ev and B. V. Svistunov, *Phys. Rev. Lett.* **81**, 2514 (1998).
- [10] K. Van Houcke, E. Kozik, N. Prokof'ev, and B. Svistunov, in *Computer Simulation Studies in Condensed Matter Physics XXI*, edited by D. Landau, S. Lewis, and H. Schuttler (Springer, Berlin, 2008).
- [11] E. Kozik, K. V. Houcke, E. Gull, L. Pollet, N. Prokof'ev, B. Svistunov, and M. Troyer, *Europhys. Lett.* **90**, 10004 (2010).
- [12] E. Kozik, M. Ferrero, and A. Georges, *Phys. Rev. Lett.* **114**, 156402 (2015).
- [13] A. A. Abrikosov, I. Dzyaloshinskii, L. P. Gorkov, and R. A. Silverman, *Methods of Quantum Field Theory in Statistical Physics* (Dover, New York, 1975).
- [14] P. Nozieres, *Theory of Interacting Fermi Systems* (Addison-Wesley, Reading, MA, 1964).
- [15] L. Hedin, *Phys. Rev.* **139**, A796 (1965).
- [16] A. N. Rubtsov, V. V. Savkin, and A. I. Lichtenstein, *Phys. Rev. B* **72**, 035122 (2005).
- [17] W. Metzner, M. Salmhofer, C. Honerkamp, V. Meden, and K. Schönhammer, *Rev. Mod. Phys.* **84**, 299 (2012).
- [18] R. E. V. Profumo, C. Groth, L. Messio, O. Parcollet, and X. Waintal, *Phys. Rev. B* **91**, 245154 (2015).
- [19] R. Rossi, F. Werner, N. Prokof'ev, and B. Svistunov, *Phys. Rev. B* **93**, 161102 (2016).
- [20] R. Blankenbecler, D. J. Scalapino, and R. L. Sugar, *Phys. Rev. D* **24**, 2278 (1981).
- [21] A.-M. S. Tremblay, B. Kyung, and D. Sénéchal, *Low Temp. Phys.* **32**, 424 (2006).
- [22] G. Sordi, P. Sémon, K. Haule, and A.-M. S. Tremblay, *Sci. Rep.* **2**, 547 (2012).
- [23] A. Macridin, M. Jarrell, T. Maier, P. R. C. Kent, and E. D'Azevedo, *Phys. Rev. Lett.* **97**, 036401 (2006).
- [24] E. Gull, O. Parcollet, and A. J. Millis, *Phys. Rev. Lett.* **110**, 216405 (2013).
- [25] This set of parameters was chosen because it leads to the largest onset temperature for the pseudogap .
- [26] A. Macridin, M. Jarrell, T. Maier, and G. A. Sawatzky, *Phys. Rev. B* **71**, 134527 (2005).
- [27] M. Chan, C. Dorow, L. Mangin-Thro, Y. Tang, Y. Ge, M. Veit, G. Yu, X. Zhao, A. Christianson, J. Park *et al.*, *Nat. Commun.* **7**, 10819 (2016).
- [28] K. L. Hur and T. M. Rice, *Ann. Phys.* **324**, 1452 (2009).
- [29] N. Furukawa, T. M. Rice, and M. Salmhofer, *Phys. Rev. Lett.* **81**, 3195 (1998).
- [30] C. Honerkamp, M. Salmhofer, N. Furukawa, and T. M. Rice, *Phys. Rev. B* **63**, 035109 (2001).
- [31] O. Parcollet, M. Ferrero, T. Ayril, H. Hafermann, I. Krivenko, L. Messio, and P. Seth, *Comput. Phys. Commun.* **196**, 398 (2015).